OXFORD JOURNAL
OF STUDENT
SCHOLARSHIP

A Physics-Based Study of Multipath Coherence in Wireless Communication Channels

Neha Abin
nehathresiaabin@gmail.com

ABSTRACT

This study looks at how reflected wireless signals affect signal stability. We built a two-dimensional computer simulation with one transmitter, one moving receiver, one direct path, and several reflected paths from objects in the environment. At each receiver position, the program adds direct and reflected electric fields while keeping track of distance, phase, and signal strength. The simulation then calculates received power, instantaneous coherence, and local coherence. The results show how movement and surrounding objects can cause interference, fading, and changes in signal stability. Instead of using only statistical fading models such as Rayleigh and Rician fading, this model calculates each path directly from the transmitter, receiver, and reflector locations. Ensemble simulations show that increasing reflector count lowers mean local coherence, while higher carrier frequencies exhibit stronger sensitivity to geometry.

Keywords: Engineering; Electrical Engineering; Wireless Communication; Multipath Propagation; Coherence

INTRODUCTION

Wireless communication depends on electromagnetic waves traveling from a transmitter to a receiver. In real environments, the signal does not usually travel in only one straight line. It can also reflect, scatter, or bend around objects before reaching the receiver. These different paths arrive with different distances, strengths, and phases. When they add together, they can make the received signal stronger or weaker. This effect is called multipath propagation, and it is one major cause of fading in wireless systems.1,4
Rayleigh and Rician fading models are useful ways to describe wireless channels, but they do not show the exact geometry that caused the fading. Rayleigh fading is used when there is no strong direct path and the received signal is made from many weak scattered parts. Rician fading is used when there is one stronger path, such as a line-of-sight path, plus other weaker scattered paths. These classical fading models statistically describe channel behavior without explicitly resolving the geometric propagation paths.2,3,4 In contrast, the present simulation takes a more direct approach by calculating the length, phase, and strength of each path from the actual positions in the model.

The physical starting point for this path-based description is classical electromagnetism. Maxwell's equations relate electric fields, magnetic fields, charge density, and current density and provide the foundation for electromagnetic-wave propagation.5,6 In a source-free, homogeneous, linear medium, they imply that time-varying electric and magnetic fields sustain one another and propagate as electromagnetic waves. Taking the curl of Faraday's law and using Ampère–Maxwell's law gives the wave equation for the electric field, $\nabla^2\mathbf{E} - (1/c^2)\partial^2\mathbf{E}/\partial t^2 = 0$ in free space, where **E** is the electric field, c is the speed of light, and t is time. For a monochromatic electromagnetic wave, the electric field can be expressed using the standard complex phasor form $\mathbf{E}(r,t) = \mathbf{E}_0 e^{j(\omega t - \mathbf{k}\cdot r + \varphi_0)}$, where r is position, $\mathbf{E}_0$ is the field amplitude, j is the imaginary unit, ω is the angular frequency, **k** is the wave vector, and φ_0 is the initial phase.7,8
Along a single propagation path of length L_p, the spatial phase term simplifies to $\mathbf{k}\cdot r = kL_p$, where $k = 2\pi/\lambda$ and λ is the wavelength. Therefore, the complex field associated with the p-th propagation path becomes

$$E_p(t) = A_p e^{j\left(\omega t - kL_p + \varphi_{p,0}\right)} \quad (1)$$

In Equation 1, $E_p(t)$ is the complex electric field for the p-th path, A_p is the path amplitude, L_p is the total propagation distance for that path, $\varphi_{p,0}$ is the initial phase of that path, and p is the path index. Equation 1 applies this path-dependent phasor notation to a single propagation component. The same notation is used throughout the manuscript so that the direct and reflected paths can be added coherently while preserving their relative phases.

As the wave propagates, its phase changes continuously with path length. This phase evolution determines whether multiple propagation paths combine constructively or destructively at the receiver.
In this paper, coherence means how similar the complex received field stays over a small change in receiver position. If the coherence is high, nearby samples have similar phase and amplitude. If the coherence is low, the signal changes quickly because the different paths are interfering with each other. This is important for high-frequency wireless systems because shorter wavelengths make the signal more sensitive to small movements and changes in geometry.

In this study, we simulated wireless wave propagation at 700 MHz, 2.4 GHz, 3.5 GHz, 6 GHz, and 28 GHz. The receiver moves through the environment while the number of reflectors changes. For each case, the model calculates the received field, received power, instantaneous coherence, and local first-order coherence. This allows the effect of frequency and reflector count to be compared using the same simulation setup.

This study is guided by the central research question: "How does increasing multipath complexity affect coherence stability in a geometry-based wireless environment?" To answer this question, we developed a deterministic propagation model that explicitly computes path lengths, phase evolution, attenuation, and coherent field addition while varying the number of reflectors and the carrier frequency. This approach allows the effect of increasing multipath complexity on coherence stability to be examined directly through the underlying geometry and wave physics rather than inferred only from statistical fading behavior.

METHODS

The propagation environment was modeled as a two-dimensional rectangular grid with dimensions 500 m by 300 m. All transmitter, receiver, and reflector coordinates are defined with respect to this grid, where the horizontal coordinate represents x-position in meters and the vertical coordinate represents y-position in meters. A fixed transmitter, a moving receiver trajectory, and a variable number of point reflectors were placed within the same coordinate domain. The reflector count, denoted by R, was used as the primary measure of multipath complexity. At each sampled receiver position, the simulation computed the direct transmitter-to-receiver distance and the reflected transmitter-to-reflector-to-receiver distances using the grid coordinates.

The transmitter was fixed at (50, 150) m. The receiver trajectory contained 4000 sample positions, with the x-coordinate varying from 100 m to 450 m and the y-coordinate following $y = 150 + 20 \sin(0.02x)$. This trajectory introduces smooth lateral displacement while maintaining a controlled path through the grid. Reflectors were placed randomly within the same two-dimensional domain. Each reflector was assigned a dimensionless reflection-strength coefficient between 0.3 and 1.0, representing the relative fraction of field amplitude retained by the reflected path after interaction with the reflector. Larger values therefore correspond to stronger reflected contributions in the coherent field sum.

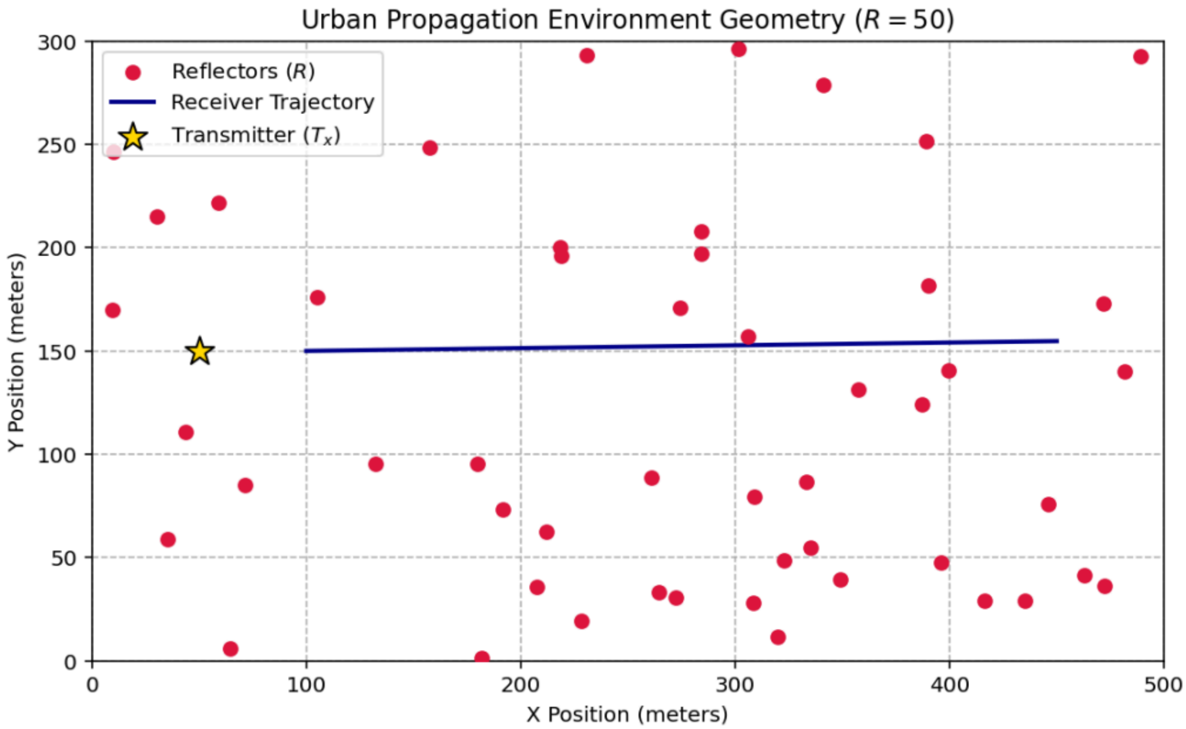

Figure 1. Example two-dimensional wireless propagation geometry used in the simulation. The modeled domain is a 500 m by 300 m rectangular coordinate grid, with all transmitter, receiver, and reflector locations specified by x- and y-position in meters. The grid structure defines the coordinate system used to compute direct and reflected path lengths at each receiver sample.

Using the grid coordinates, the total reflected path length for each reflector was calculated as the distance from the transmitter to the reflector plus the distance from the reflector to the receiver. The direct transmitter-to-receiver path was included separately, allowing the total received field to be formed by coherent superposition of the direct and reflected components. Because the wavelength and wave number were already defined in the Introduction, these path lengths directly determine the phase accumulated by each propagation component.

$$E_i(x) = A_i(x)e^{j\phi_i(x)} \tag{2}$$

Equation 2 expresses each reflected contribution using the phasor notation introduced earlier. In this expression, $E_i(x)$ is the complex electric field from the i-th reflected path at receiver position x, $A_i(x)$ is its position-dependent amplitude, $\varphi_i(x)$ is its accumulated phase, and i is the reflector-path index. The exponential factor accounts for the phase rotation accumulated as the reflected path length changes with receiver position.

$$\phi_i(x) = -\, k\, d_{total,i}(x) \tag{3}$$

Equation 3 relates the propagation phase to the geometry-dependent path length using the same traveling-wave convention introduced in the Introduction. In this equation, $\varphi_i(x)$ is the phase of the i-th reflected path, k is the wave number, and $d_{total,i}(x)$ is the total transmitter-to-reflector-to-receiver distance for that path at receiver position x.

$$A_i(x) = \frac{P_i}{d_{total,i}(x)} \tag{4}$$

In free-space propagation, the electric-field amplitude decreases approximately in proportion to the inverse of propagation distance, whereas received power decreases approximately as the inverse square of distance.5,7 Because the present model computes coherent addition of complex electric fields rather than received powers, each reflected-path amplitude is modeled as inversely proportional to the total propagation distance. In Equation 4, $A_i(x)$ is the amplitude of the i-th reflected path at receiver position x, P_i is a dimensionless reflection-strength coefficient representing the relative field amplitude retained after reflection, and $d_{total,i}(x)$ is the total reflected propagation distance. Each reflector was assigned a dimensionless reflection-strength coefficient, P_i, randomly selected between 0.3 and 1.0. This range represents moderately weak to strong reflected signals and provides a realistic range of reflection strengths. Because the model does not include material properties or reflection angles, P_i is treated as a simplified parameter rather than an exact physical reflection coefficient. This simplified attenuation model captures the dominant distance-dependent reduction of field magnitude while keeping the propagation model computationally tractable.

Combining the attenuation and phase relations gives the numerical reflected-field form used in the simulation: $E_i(x) = [P_i/d_{total,i}(x)]\ \exp[-jkd_{total,i}(x)]$. This expression is not treated as a separate governing equation.Thus, each reflected contribution is evaluated from its total transmitter-reflector-receiver path length before being added to the direct field.This representation is appropriate for a narrowband free-space propagation path in which amplitude attenuation and phase accumulation are modeled separately.

The total received field is the complex electric field at the receiver after coherent addition of the direct and reflected propagation components. Because the phase of each component depends on its propagation distance, the total field can increase through constructive interference or decrease through destructive interference. The received power was computed from the squared magnitude of this total complex field. We also defined an instantaneous coherence metric that compares the magnitude of the coherently summed field with the maximum possible magnitude obtained if all path contributions were perfectly phase aligned.

$$E_{total}(x) = E_{direct}(x) + \sum_{i=1}^{R} E_i(x) \tag{5}$$

Equation 5 defines the coherent received field as the sum of the direct component and all R reflected components. In this equation, $E_{total}(x)$ is the total complex electric field at receiver position x, $E_{direct}(x)$ is the direct transmitter-to-receiver field, R is the number of reflected paths or reflectors, and $E_i(x)$ is the i-th reflected contribution. Because the summation is performed over complex fields rather than powers, the model retains phase information and captures both constructive and destructive interference.

$$C(x) = \frac{|E_{total}(x)|}{|E_{direct}(x)| + \sum_{i=1}^{R} |E_i(x)|} \tag{6}$$

Equation 6 defines the instantaneous coherence metric C(x). In this expression, $|E_{total}(x)|$ is the magnitude of the coherently summed electric field, $|E_{direct}(x)|$ is the magnitude of the direct component, and $|E_i(x)|$ is the magnitude of each reflected component. The denominator represents the largest possible field magnitude if all components were perfectly phase aligned. Values near one indicate that the paths are nearly phase aligned, while smaller values indicate destructive interference and reduced instantaneous coherence.

For the reflected paths, the phase was computed directly from the geometry-dependent path length using the relation $\varphi_i(x) = kd_{total,i}(x)$, where k is the wave number, $d_{total,i}(x)$ is the total reflected path distance, and x is the receiver position along the trajectory. This definition was used internally in the reflected-field calculation rather than treated as a separate governing equation.

The propagation distance of each multipath component was modeled geometrically as the sum of the transmitter-to-scatterer distance and the scatterer-to-receiver distance: $d_{total,i}(x) = d_{T,i} + d_{i,R}(x)$. Here, $d_{total,i}(x)$ is the full reflected path length for the i-th reflector, $d_{T,i}$ is the distance from the transmitter to that reflector, and $d_{i,R}(x)$ is the distance from the reflector to the receiver at position x. This inline definition avoids introducing a separate displayed equation for a quantity that is immediately substituted into the reflected-field calculation.

Local first-order coherence, written as $g^{(1)}(x;\tau)$, was used to quantify short-range stability of the complex received field. This is based on the standard first-order coherence function from statistical optics; the new computational element in this study is the moving-window implementation along the receiver trajectory.9,10 In this notation, x is the receiver position, τ is the separation lag between two nearby receiver samples, the superscript (1) indicates first-order field coherence, and the angle brackets in

Equation 7 represent averaging over a finite sliding window. Whereas instantaneous coherence is evaluated at a single receiver position, local coherence compares the field at nearby positions separated by τ and averages that comparison over the window. In this study, $\tau = 20$ samples was chosen to probe decorrelation over a short spatial separation along the receiver trajectory, while the 120-sample window provided enough neighboring samples to smooth rapid point-to-point interference without eliminating local channel variations. A smaller τ would measure more immediate similarity and generally produce larger coherence values, while a larger τ would test longer-range similarity and would be more sensitive to rapid phase variation. Similarly, a shorter window would preserve sharper local changes but be noisier, whereas a longer window would provide smoother estimates at the cost of reduced spatial resolution. The values of $\tau = 20$samples and a 120-sample window were chosen empirically to balance smoothing and local detail. They were not selected from a specific physical length scale, and a detailed parameter sensitivity study is left for future work.

$$g^{(1)}(t;\tau) = \frac{|\langle E^{*}(t')E(t'+\tau)\rangle|}{\sqrt{\langle|E(t')|^{2}\rangle\langle|E(t'+\tau)|^{2}\rangle}} \tag{7}$$

The averaging operation in Equation 7 was performed over the 120 receiver-position samples contained in the local sliding window centered around the evaluation point. Instantaneous coherence therefore captures point-by-point interference effects, while local coherence provides a smooth measure of whether the channel remains predictable over a short spatial interval. The simulation outputs included received power, instantaneous coherence, and local first-order coherence for each receiver position.

The analysis was performed at two levels. First, a single seed and iteration were used to visualize the detailed field evolution along one receiver trajectory, including coherence, received power, and propagation geometry. Second, a Monte Carlo ensemble was used to evaluate aggregate statistics across randomized reflector configurations. For the ensemble study, reflector counts R = {2, 4, 8, 12, 16, 24, 50, 100, 200, 400} were tested using 100 random seeds for each case. The summary quantities were the mean local coherence, the minimum local coherence, and the maximum sustained coherence cliff. The sustained coherence cliff was defined by comparing the average local coherence before and after a candidate receiver position, rather than by using only the largest adjacent-sample drop. For each position x_i, the average local coherence in a pre-window was subtracted from the average local coherence in a post-window, and the largest positive decrease across the trajectory was reported as the maximum sustained coherence cliff.

Mathematically, if $g_i = g^{(1)}(x_i;\tau)$ is the local first-order coherence at sample i, the mean coherence before a candidate point is defined as $\langle g\rangle_{before}(x_i) = (1/M_{pre})\Sigma_{m=1}^{Mpre} g_{i-m}$, and the mean coherence after that point is defined as $\langle g\rangle_{after}(x_i) = (1/M_{post})\Sigma_{m=0}^{Mpost-1} g_{i+m}$. The sustained cliff strength is then $\Delta g_{cliff}(x_i) = \langle g\rangle_{before}(x_i) - \langle g\rangle_{after}(x_i)$, and the reported maximum sustained coherence cliff is $C_{sustained} = \max_i \Delta g_{cliff}(x_i)$. This definition identifies a transition from a locally high-coherence region to a persistently lower-coherence region.

This computational design allowed the channel behavior to be examined at two levels: detailed field evolution within a single realization and aggregate coherence statistics across many random reflector configurations. As a result, the manuscript can distinguish deterministic geometry effects along one path from the statistical effect of increasing reflectors across the Monte Carlo ensemble.

RESULTS AND DISCUSSION

The simulation produced two categories of results. The single-realization results show how the direct and reflected paths combine to determine received power, instantaneous coherence, and local coherence along one receiver trajectory. The Monte Carlo ensemble study over randomized reflector configurations results show how the same coherence metrics change statistically as reflector count increases.

In the single-run coherence results shown in Figure 2, the instantaneous coherence C(x) changes rapidly because it depends on the exact phase alignment of the direct and reflected components at each receiver position. Even small changes in path length can shift the relative phases and produce strong constructive or destructive interference. The local coherence $g^{(1)}(x;\tau)$ varies more smoothly because it averages field similarity over a local window, making it a more stable indicator of short-range channel predictability.

The received-power behavior in Figure 3 follows from the magnitude of the total coherently summed field. As the receiver moves from x = 100 m to x = 450 m with a lateral displacement defined by y = 150 + 20 sin(0.02x), the direct and reflected propagation distances change continuously. The resulting power variation contains both the general attenuation associated with increasing path length and the finer fading structure produced by multipath interference.

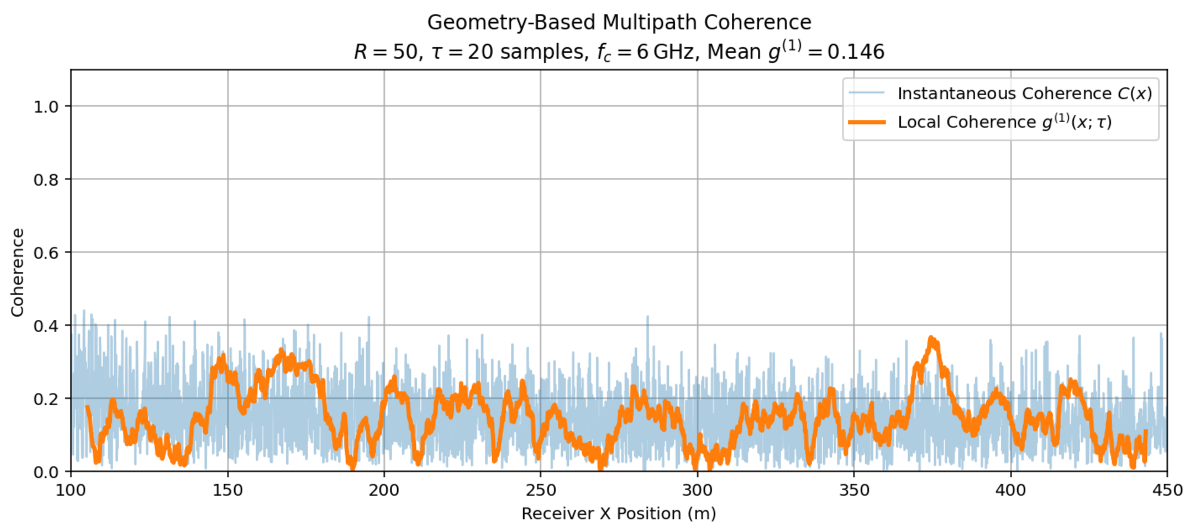

Figure 2. Instantaneous coherence and local first-order coherence for a single simulation realization. The figure shows that instantaneous coherence changes rapidly from point to point, while local first-order coherence gives a smoother view of nearby channel stability.

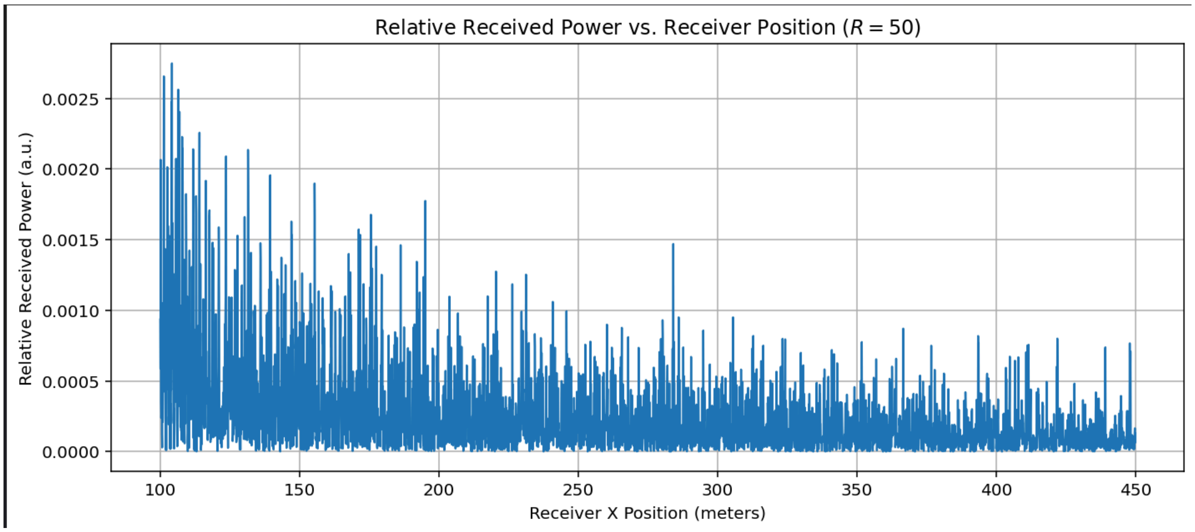

Figure 3. Received field power across the spatial receiver trajectory. The overall downward trend is related to distance attenuation, while the smaller fluctuations are caused by constructive and destructive multipath interference.

For each reflector count, the simulation was repeated over 100 independent random reflector realizations. Mean local coherence measures the typical short-range field similarity along the receiver trajectory, minimum local coherence identifies the weakest local stability encountered in a realization, and the maximum sustained coherence cliff measures the largest transition from a high-coherence region to a persistently lower-coherence region. Error bars represent the standard error of the mean (SEM = SD/√N) computed from the 100 Monte Carlo realizations.

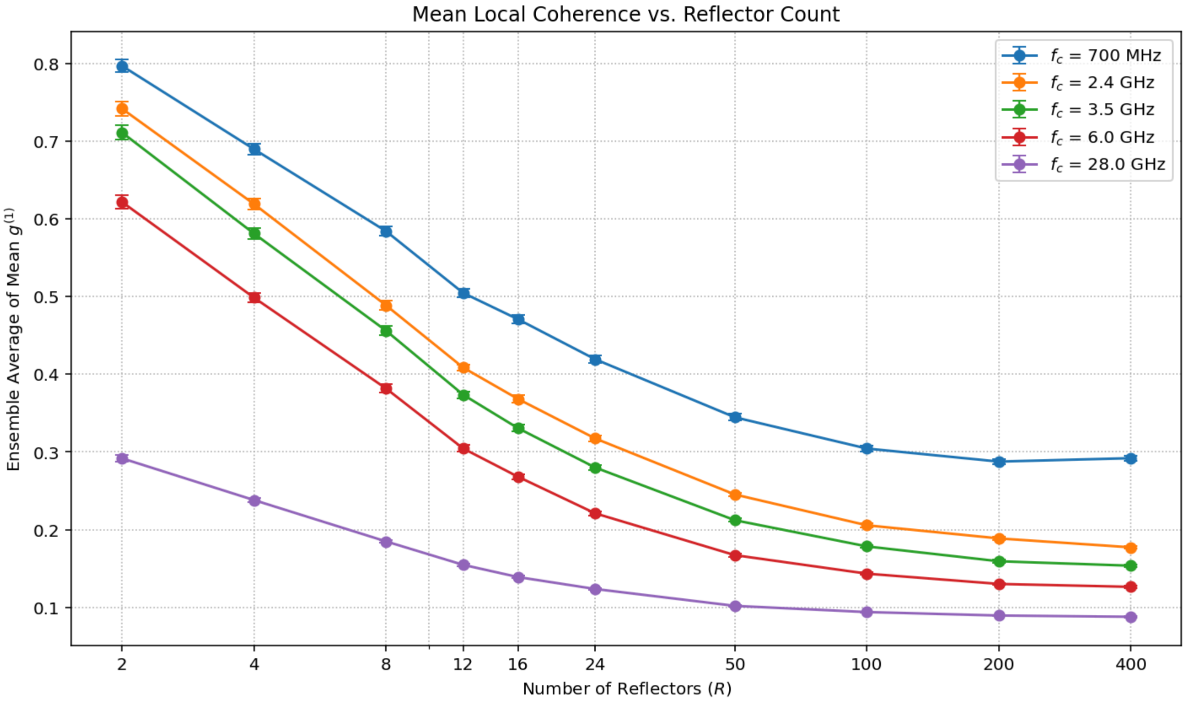

Figure 4 presents the primary result of this study. The ensemble-average mean local coherence decreases systematically as the reflector count increases for every carrier frequency, demonstrating that increasing multipath complexity progressively reduces short-range channel predictability. This trend is consistent with the increasing number of reflected propagation paths producing larger phase diversity and more frequent destructive interference.

The reduction is strongest at higher carrier frequencies. At R=400, the mean local coherence is approximately 0.40 at 700 MHz, compared with approximately 0.11 at 28 GHz, while the intermediate frequencies fall between these limits. Thus, under the same geometric scattering conditions, the 28 GHz channel retains only about one-quarter to one-third of the local coherence observed at 700 MHz.

The separation between the frequency curves becomes progressively larger as reflector count increases, indicating that higher-frequency wireless channels are substantially more sensitive to multipath geometry than lower-frequency systems. For example, the 700 MHz curve decreases gradually from approximately 0.80 at R=2 to 0.40 at R=400, whereas the 28 GHz curve decreases from approximately 0.30 to 0.11 over the same range. This behavior demonstrates that higher-frequency propagation experiences much faster coherence degradation as scattering complexity increases. These findings have direct implications for 5G FR2 and future 6G systems, where shorter wavelengths require more frequent channel estimation, beam tracking, and beam refinement to maintain reliable communication links in dense scattering environments.

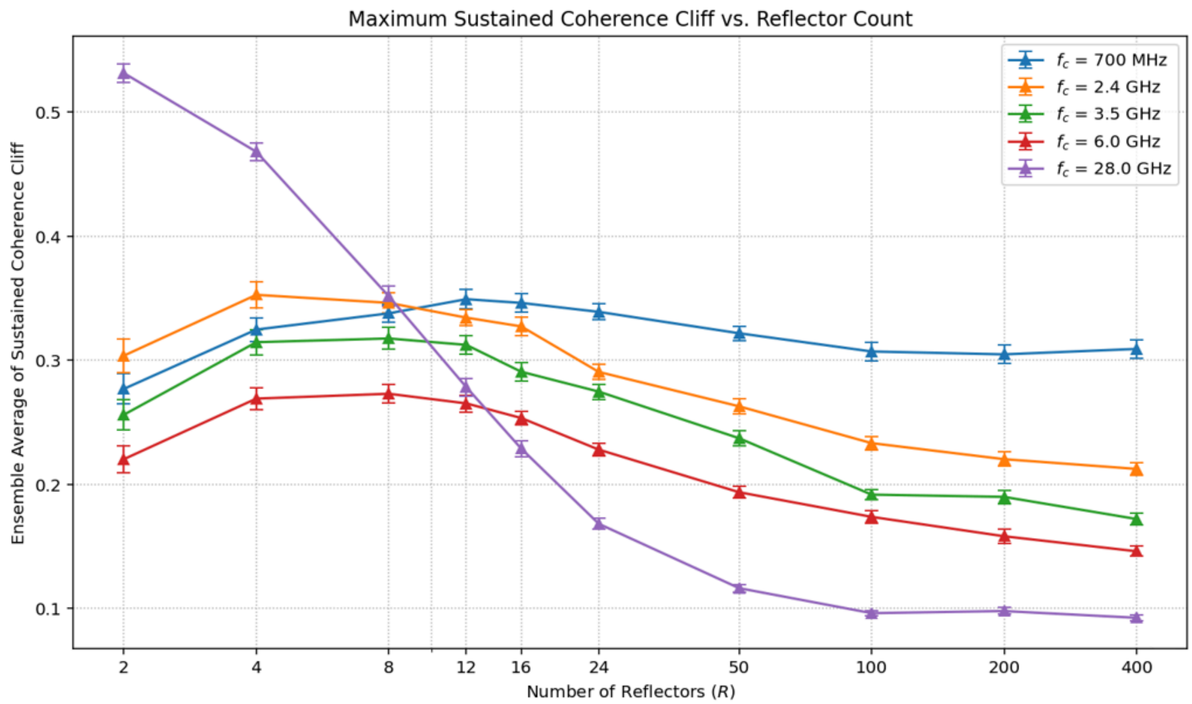

Figure 5. Multi-frequency ensemble average of the maximum sustained coherence cliff as a function of reflector count. The curves show that sustained coherence cliffs are strongest at intermediate multipath complexity. At very high reflector counts, the channel may become continuously decorrelated rather than undergoing isolated transitions. Error bars represent the standard error of the mean (SEM = SD/√N) computed from 100 independent Monte Carlo realizations. The 28 GHz channel exhibits the largest coherence cliffs at low reflector counts but decreases rapidly as multipath complexity increases. Because the wavelength is much shorter, small path-length differences produce much larger phase changes, causing the channel to become continuously decorrelated rather than undergoing isolated coherence transitions

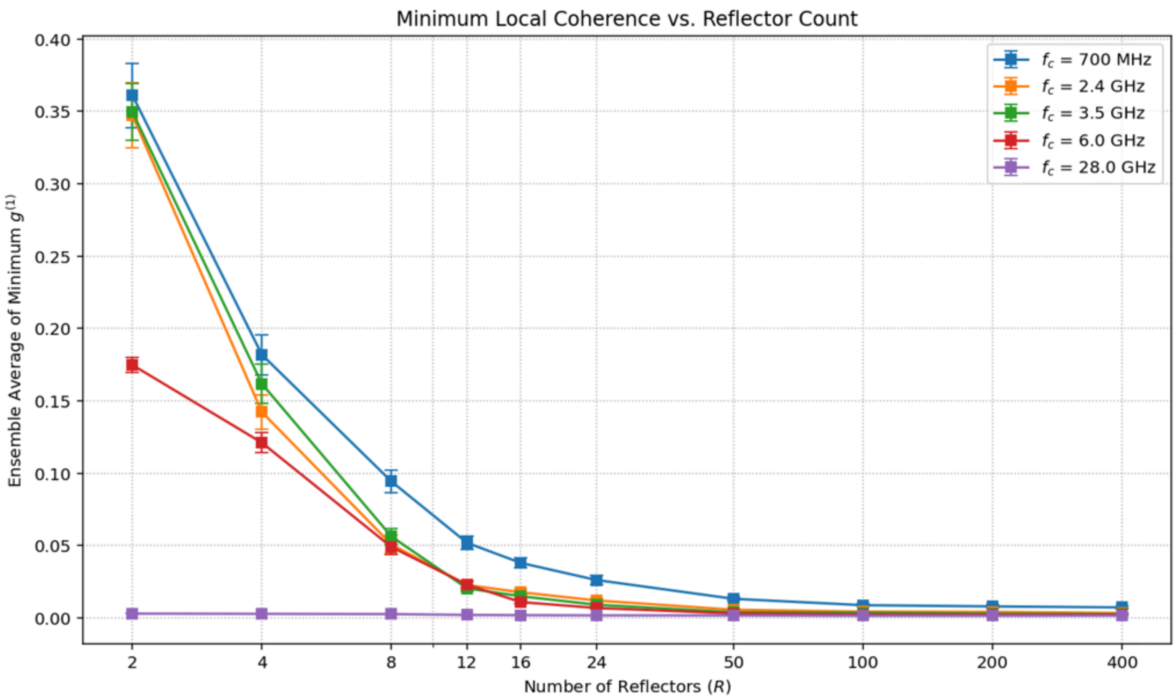

Figure 6. Minimum local coherence as a function of reflector count for the tested carrier frequencies. Lower values show receiver locations where the channel becomes strongly decorrelated. Error bars represent the standard error of the mean (SEM = SD/√N) computed from 100 independent Monte Carlo realizations.

The minimum-coherence results emphasize the worst local stability encountered during propagation. As R increases, the probability of encountering a receiver location with severe destructive interference and rapid decorrelation also increases. The frequency dependence is again strongest at higher carrier frequencies because shorter wavelengths convert the same geometric displacement into a larger phase change.

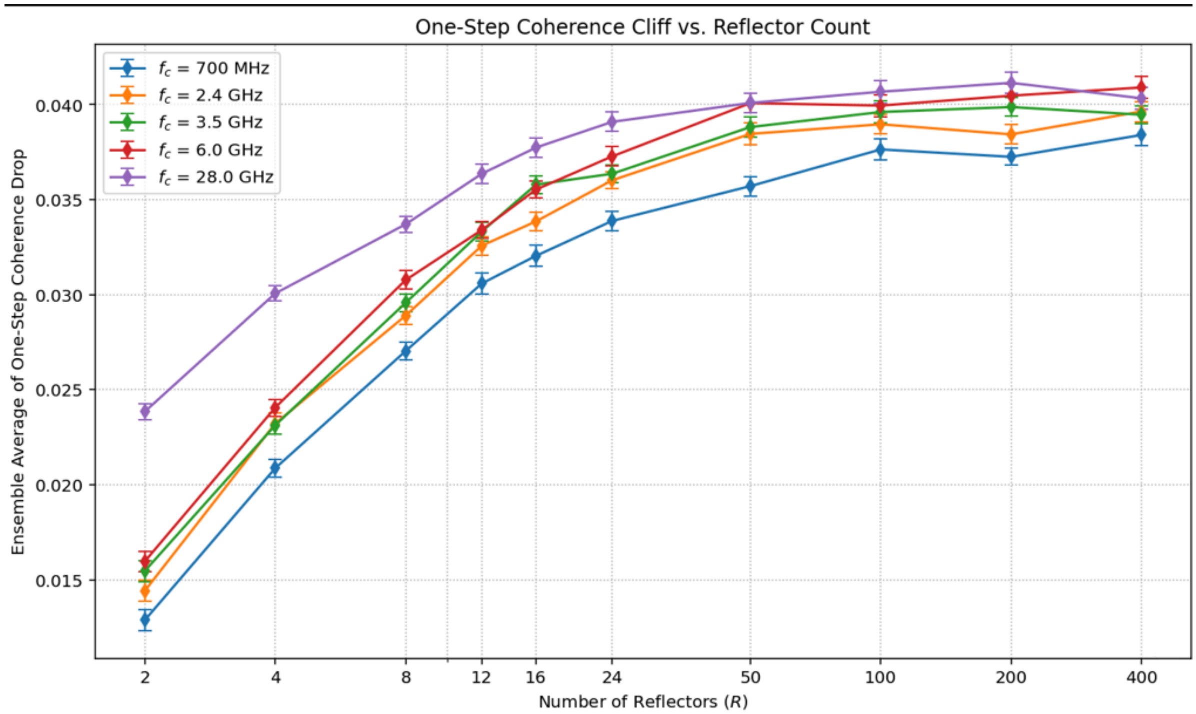

Figure 7. One-Step Coherence Cliff vs. Reflector Count. This metric tracks the largest single-step local downward drop and serves as a secondary numerical diagnostic tool rather than a measure of sustained propagation regime changes.

The sustained-cliff metric adds information that is not captured by mean or minimum coherence alone. Two channels may have similar mean coherence, but one may vary gradually while the other undergoes a clear transition from high local coherence to lower local coherence over a finite region of the receiver trajectory. The increase in maximum sustained coherence cliff with R indicates that dense multipath environments are more likely to produce persistent coherence losses, which is important for mobile receivers because sustained coherence degradation can affect channel estimation, beam tracking, and link reliability.

LIMITATIONS

This study employs several simplifying assumptions that make the model interpretable but limit direct comparison with real propagation environments. The simulation is two-dimensional, so it does not capture elevation-dependent effects, three-dimensional scattering, antenna height, or vertical building structure. Reflectors are represented as ideal point scatterers with constant reflection-strength coefficients, whereas real surfaces have material-dependent reflection, absorption, roughness, and angular scattering properties. The attenuation model uses an idealized inverse-distance field dependence and does not include shadowing, diffraction around obstacles, polarization mismatch, atmospheric absorption, antenna radiation patterns, or frequency-selective delay spread. The receiver trajectory is prescribed rather than generated from a realistic mobility model, and the reflectors remain static. Finally, the Monte Carlo ensemble provides statistical trends over random reflector placements, but larger sample sizes and extended reflector counts would reduce uncertainty and strengthen claims about convergence at high multipath complexity.

FUTURE WORK

Future work should extend the present model in several directions. First, the Monte Carlo sample size should be increased so that error bars decrease and ensemble averages become more reliable. Second, more realistic propagation physics should be incorporated, including material-dependent reflection coefficients, diffraction, blockage, polarization, antenna gain patterns, and frequency-selective multipath delays. Third, the geometry can be generalized from a two-dimensional grid to realistic urban, suburban, and indoor environments using measured or map-based building layouts. Finally, additional metrics such as dominant-path fraction, path entropy, delay spread, coherence bandwidth, and machine-learning-based coherence prediction could help connect the present physics-based framework to practical wireless-system design.

CONCLUSION

This study built a physics-based simulation to study multipath coherence in wireless communication channels. The model adds together a direct path and several reflected paths. Each path has its own distance, phase, and amplitude based on the geometry of the transmitter, receiver, and reflectors. By changing the number of reflectors and the carrier frequency, the simulation shows how multipath affects received power and coherence.

The results show that small receiver movements can cause large changes in the received field because path-length changes also change the phase of each signal component. Instantaneous coherence changes quickly from point to point, while local first-order coherence gives a smoother view of short-range stability. In the Monte Carlo results, adding more reflectors generally lowers coherence and makes sustained drops in local coherence more likely.

The frequency-dependent analysis further shows that higher carrier frequencies are more sensitive to geometry because shorter wavelengths produce faster phase variation for the same physical displacement. This finding is especially relevant for modern high-frequency wireless systems, including upper mid-band and millimeter-wave networks. Overall, the manuscript demonstrates that a geometry-based propagation model can provide physical insight into fading, interference, and coherence degradation beyond what is visible from statistical fading models alone.

AI ACKNOWLEDGEMENT

During the preparation of this work, the authors used AI assistance to improve language readability, organize formatting, and check the manuscript against the IJHSR template. After using this tool, the authors reviewed and edited the content as needed and take full responsibility for the content of the publication.

ACKNOWLEDGEMENT

The authors thank the mentor, teacher, and school community for their guidance and support during this research project.

REFERENCES

1. T. S. Rappaport, *Wireless Communications: Principles and Practice*, 2nd ed. Prentice Hall, 2002.
2. R. H. Clarke, "A Statistical Theory of Mobile-Radio Reception," *Bell System Technical Journal*, vol. 47, no. 6, pp. 957–1000, 1968.
3. W. C. Jakes, *Microwave Mobile Communications*. Wiley, 1974.
4. A. Goldsmith, *Wireless Communications*. Cambridge University Press, 2005.
5. D. J. Griffiths, *Introduction to Electrodynamics*, 4th ed. Cambridge University Press, 2017.
6. D. Halliday, R. Resnick, and J. Walker, *Fundamentals of Physics, Volume 2*, 11th ed. Wiley, 2019.
7. M. Born and E. Wolf, *Principles of Optics*, 7th ed. Cambridge University Press, 1999.
8. E. Hecht, *Optics*, 5th ed. Pearson, 2017.
9. J. W. Goodman, *Statistical Optics*, 2nd ed. Wiley, 2015.
10. L. Mandel and E. Wolf, *Optical Coherence and Quantum Optics*. Cambridge University Press, 1995.

AUTHOR INFORMATION

Neha Abin is a Junior high school student in Allen high school, Texas and she is interested in physics, engineering, and wireless communication. This research project explores how wave interference and multipath propagation affect wireless signal stability.